Supplementary Information

Vasily V. Temnov,[*,†,‡] Alexandr Alekhin,[‡,¶] Andrei Samokhvalov,[†] Dmitry S. Ivanov,[†,§] Alexey M. Lomonosov,[‖] Paolo Vavassori,[¶,⊥] Evgeny Modin,[¶] and Vadim P. Veiko[†]

†*ITMO University, 197101 St. Petersburg, Russia*

‡*IMMM CNRS 6283, Le Mans Université, 72085 Le Mans, France*

¶*CIC nanoGUNE BRTA, E-20018 Donostia-San Sebastian, Spain*

§*Department of Physics and OPTIMAS Research Center, Technical University of Kaiserslautern, 67663 Kaiserslautern, Germany*

‖*Prokhorov General Physics Institute of the Russian Academy of Sciences, 119991 Vavilova str. 38 Moscow Russia*

⊥*IKERBASQUE, Basque Foundation for Science, E-48013 Bilbao , Spain*

E-mail: vasily.temnov@univ-lemans.fr

Morphology of fs-laser-fabricated nanostructures in thin nickel films

In order to identify the appropriate sample thickness for our case study, we have performed some reference experiments on 100-nm nickel films on glass. Inline with Fig. 1 and Fig. 2 in the manuscript, Fig. S1 summarizes the results of microscopic characterization of fs-laser-produced structures obtained for different pulse energies (fluences). As in the case of 300 nm nickel thin films, the thermo-mechanical process of spallation manifests itself in formation of quasi-free-standing spallation flakes for fluence F significantly exceeding the spallation

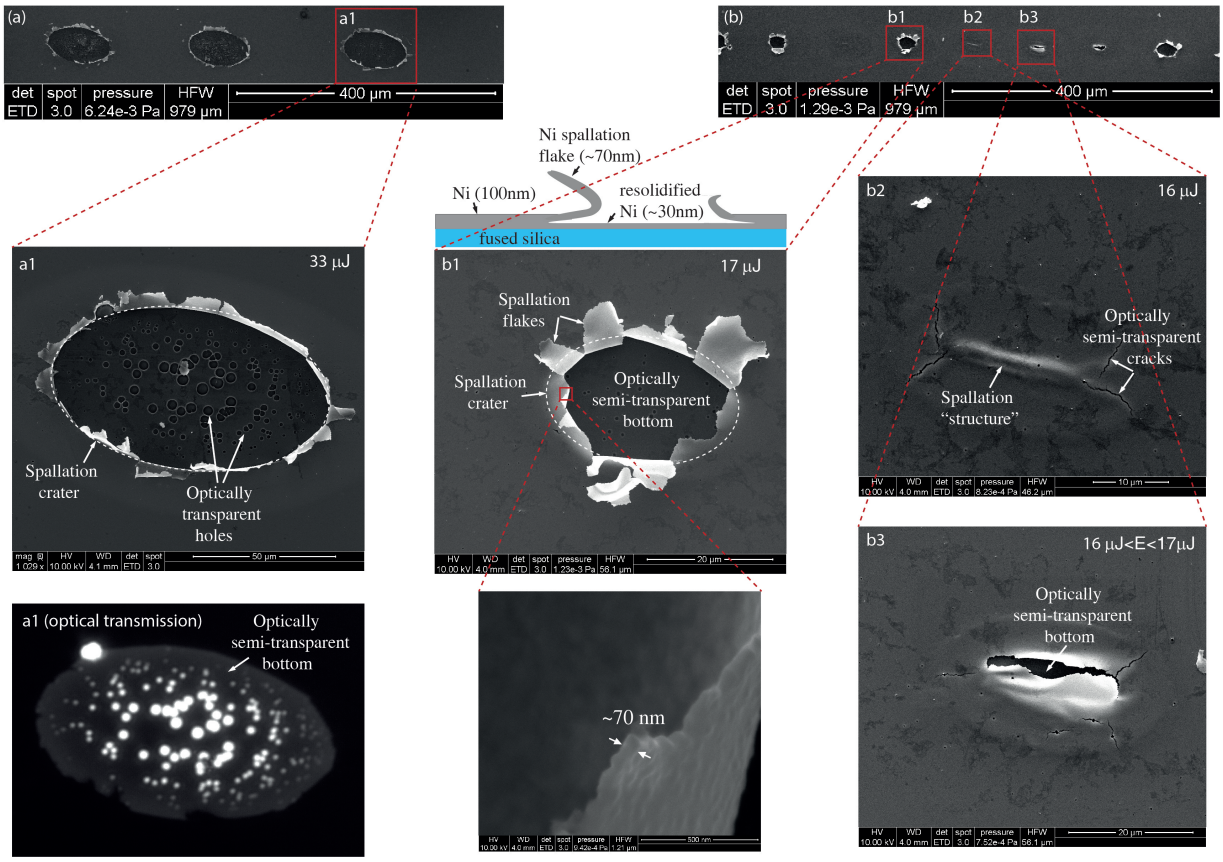

Figure S1: Spallation experiments on 100 nm Nickel films on glass. (a) Similar elliptical spallation craters are produced by 33 μJ pulses with peak fluence F=520 mJ/cm^2 (2 times larger than the spallation threshold). These craters are characterized by numerous optically transparent holes in the semi-transparent bottom, see crater $a1$. (b) In the vicinity of the spallation threshold (a few percent above or below) irregular spallation structures are produced in the form of small elliptical spallation craters ($b1$, pulse energy 17 μJ, $F \simeq 1.08\ F_{spall}$), pencil-like spallation structures surrounded by cracks ($b2$, pulse energy 16 μJ,$F \simeq F_{spall}$) or elongated wide spallation cracks ($b3$, pulse energy between 16 and 17 μJ, fluences between F_{spall} and 1.08 F_{spall}). The thickness of the spalled layer on structure $b1$ is approximately 70 nm.

threshold $F_{spall} = (250 \pm 25)$ mJ/cm^2 for 100 nm nickel films (which is approximately two times smaller as compared to 300 nm films). Fig. S1(a) shows the SEM images of several structures produced with 33 μJ laser pulses (peak fluence $\simeq 2\ F_{spall}$). The zoom-in in structure (a1) demonstrates a clear elliptical spallation crater. The bottom of the crated is optically semi-transparent and perforated with a number of optically transparent holes, which can be clearly seen in the optical transmission image of the structure (a1). The diameter and surface density of holes is larger in the central area corresponding to larger fluence. Being focused on the spallation mechanism, we have inspected the structures produced in the vicinity of the spallation threshold (pulse energy of 16 μJ). Figure 1(b) features a series of structures produced with an average pulse energy of 17 μJ, i.e. just a few percent above the spallation threshold. Due to the shot-to-shot fluctuations of the pulse energy the related damage area can be classified in two groups. The first group of structures represents open structures with quasi-free-standing spallation flakes, see structure $b1$ obtained by with a 17 μJ pulse. The elliptical spallation area is clearly visible and the thickness of the spalled layer is estimated to be around 70 nm. Therefore we conclude that 30 nm remained on the surface, a conclusion consistent with an observation that the bottom of the spallation crater is semi-transparent for visible light. The second group of structures with complex morphology represents either by narrow pencil-like spallation structures parallel to the long axis of the ellipse and surrounded by a few optically semi-transparent cracks ($b2$, pulse energy 16 μJ) or long wide cracks opening up on top of semi-transparent bottom (structure $b3$, pulse energy between 16 and 17 μJ). These empirical observations suggest that closed spallation cavities in 100-nm nickel films are too hard to be reliably obtained under given focusing conditions.

Considering now 300-nm nickel films on glass, the sketches for *flat-top* and *M-shaped* spallation cavities in Fig. 3 and Fig. 4 in the main manuscript have been inferred by interferometric measurements, using information from the SEM images of open spallation flakes in Fig. 2. In order to achieve a direct verification of our ansatz, we have performed precision ion beam milling of the structure using the focused ion beam (FIB) followed by

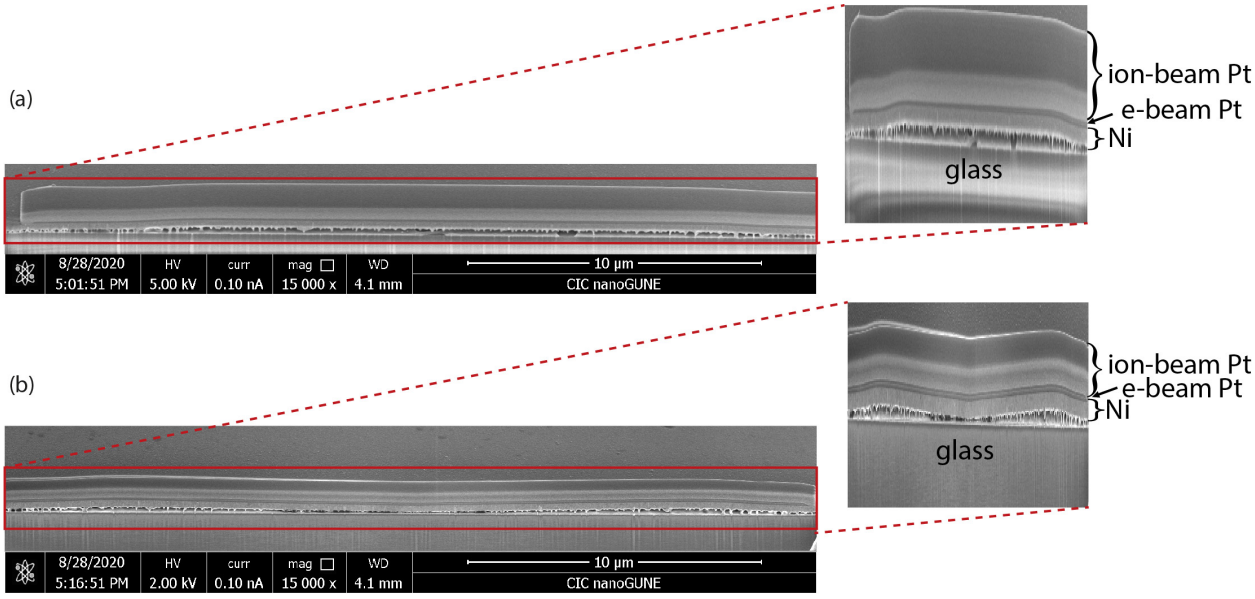

Figure S2: Closed spallation cavities similar to those in Fig. 3 in the manuscript have been cut (along the dashed lines in Fig. 3) using the focused ion beam and observed with the SEM from the side. Presented SEM images confirm (a) *flat-top* and (b) *M-shaped* internal structures sketched in Fig. 2 in the main manuscript.

high resolution SEM imaging of structure cross sections. Prior to FIB-cutting, spallation cavities have been covered with a thin layer of Pt, initially using electron beam-induced deposition followed by a thicker Pt layer deposited by ion-beam induced deposition. The initial step was essential for preventing the surface of the nickel film from damage during the thick protective Pt-layer deposition. Another advantage of using e-beam deposited Pt layer is that it provides good contrast at the interface of Ni-film and ion-deposited Pt layer. Both protective layers allow to preserve the initial surface and prepare a clean and sharp FIB cut. The SEM images of the cross-sections, presented in Fig. S2, were obtained using a Helios NanoLab 450S (ThermoFisher) at the accelerating voltage of 2–5 kV and the beam current of 50-100 pA. Thus, we have performed direct experimental observation of *flat-top* and (b) *M-shaped* internal structures sketched in Fig. 2 of the main manuscript.

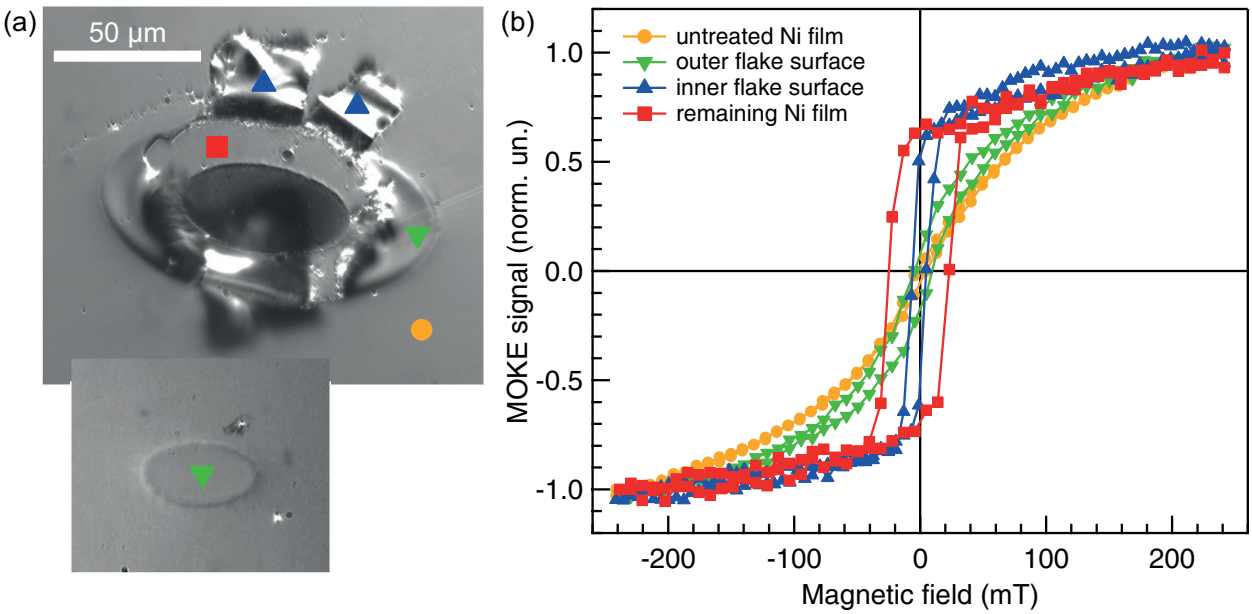

Figure S3: Magneto-optical characterization of fs-laser-produced nanostructures. Panel (a) presents optical images of an ablation crater (upper image) and a closed cavity (lower image). Panel (b) shows the hysteresis loops measured at the different positions depicted with the corresponding markers. In each measurement the MOKE signal was acquired from a circular area with the diameter of 10 μm.

Magneto-optical properties of produced nanostructures

In order to understand the impact of fs-laser-nanostructuring on the magneto-optical properties of nickel forming closed spallation cavities, we have performed magneto-optical Kerr effect (MOKE) measurements at different points on the sample corresponding to different parts of open ablation spallation flakes, the ring outside the ablation crater, and the top of closed spallation cavities. MOKE measurements were performed utilizing an optical wide-field polarization microscope optimized for Kerr microscopy (Evico Magnetics GmbH, Germany[1]). The microscope is equipped with an electromagnet that allows the application of a magnetic field of up to 500 mT along an arbitrary direction in the sample plane and with a high sensitivity CCD camera that is capable of taking magnetic-contrast images of the sample surface with a spatial resolution of the order of the micrometer. The key feature of our approach is that we can measure the field-dependent local magnetization, i.e. a local hysteresis loop at an arbitrary region of interest, choosing its shape, size, and position in

the field of view. The measurement is performed by means of a reduced number of pixels within the CCD camera array, which is used as a conventional light intensity detector.[2] The results presented in Fig. S3 indicate that the magnetic hysteresis loops on the outer surface of spallation flakes and on the closed spallation cavity are nearly identical to those measured on unexcited nickel surface. Such hysteresis loops are typical for a random orientation of large grains with strong magnetic anisotropy. These results corroborate our conclusion that the outer part was not severely affected by laser excitation. The inner part of spallation flakes and the resolidified nickel exhibit markedly different loops with high remanence (magnetization value at zero applied field) and sharp transitions (magnetization reversal) typical for a magnetic thin film with negligible magnetic anisotropy. These differences reflect the distinct crystal structure of the nickel film in the different regions, as it was also observed in the SEM cross sections (see, for example, Fig. 4 in the main manuscript): large grains which are present in the unexcited part of the Ni film and in the outer surface of spallation cavities; much smaller grains in the resolidified Ni inside the cavities.

Elastic properties of spallation cavities

Figure S4 presents the results of the theoretical and experimental studies of the elastic properties of the spallation cavities. In the latter case, the investigation was performed with the help of an optical pump-probe technique, where a single spallation cavity was pumped and probed by femtosecond laser pulses at 800 nm and 400 nm wavelength, respectively. Variations of the linear reflectivity signal were recorded as a function of the temporal delay between pump and probe pulses up to 8 nanoseconds (see Fig. S4(b)). Just after the laser excitation, the linear reflectivity rapidly changes on a picosecond time scale due to the increase of the electron and lattice temperatures. The subsequent heat diffusion is evidenced by the decrease of the reflectivity on a sub-nanosecond time scale. Laser-induced thermal stresses in Ni result in the excitation of a long-living vibration mode of the spallation cavity

evidenced by the appearance of large-amplitude oscillations of reflectivity at a frequency of 0.22 GHz.

Vibration modes of spallation cavities were calculated numerically, by means of the finite-element method (FEM). Geometrical parameters for the model were chosen in accordance to the cross-sections in Fig. 4(e) in the manuscript. Two kinds of calculations were performed: search for the eigenmodes of the periodic structure of cavities, and calculation of the response of the periodic structure to a sinusoidal perturbation which frequency was swept within the range of interest. The source for the latter method simulated the thermoelastic stress induced by a temperature rise within a thin nickel layer due to the light absorption. The result shows the modes that can be excited in the experiment only, and gives us the idea of their relative magnitudes. The mode in Fig. S4(a) corresponds to the experimentally observed oscillation in the reflectivity signal (see Fig. S4(b)). This mode can be interpreted as a half-wave resonance of an antisymmetric wave of the Lamb type. Correspondingly, we expect smaller cavities to exhibit high-frequency acoustic response entering the GHz frequency range and, therefore, being interesting for integrated 2D-devices for ultrafast opto-acoustic modulation.

Molecular dynamics simulations for femtosecond and picosecond laser pulses

For a deeper fundamental understanding of the spallation process, detected in the experiments, we performed the atomistic-continuum modeling of a 100 fs laser pulse interaction with a 300 nm Ni film situated on a silica substrate and the laser pulse is irradiating the target through the substrate (see Fig. S5(a)). Complementary simulations for 30 ps long laser pulses (see Fig. S5(b)) aimed to quantify the properties of thermo-acoustic spallation with longer laser pulses.

The model is based on the Molecular Dynamics (MD) approach, but it also accounts for thermal conductivity of laser-excited free carriers in metals due to the integrated Two Tem-

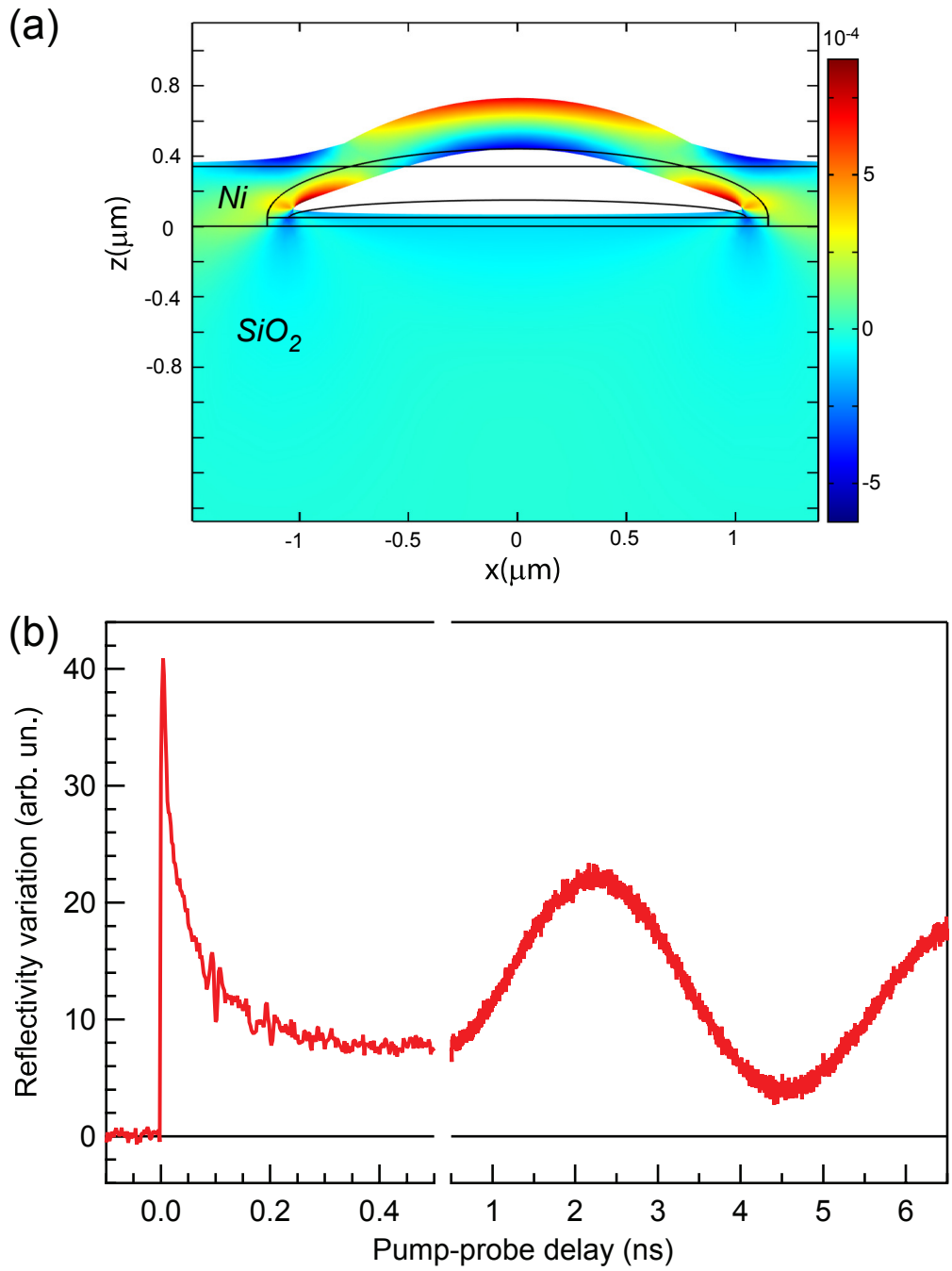

Figure S4: Acoustic response of spallation cavities, presented in Fig. 4 of the main manuscript. (a) The calculated lowest-order acoustic vibration mode of the spallation cavity with the dimensions taken from Fig. 4 occurs at a frequency of 0.2 GHz. The color image displays the spatial strain distribution of the mode. (b) This acoustic vibration is seen in the time-resolved reflectivity measurements performed on a single spallation cavity: ultrafast laser heating and heat diffusion on a picosecond time scale are followed by slow oscillating behavior of the reflectivity signal on a nanosecond time scale at a frequency of 0.22 GHz.

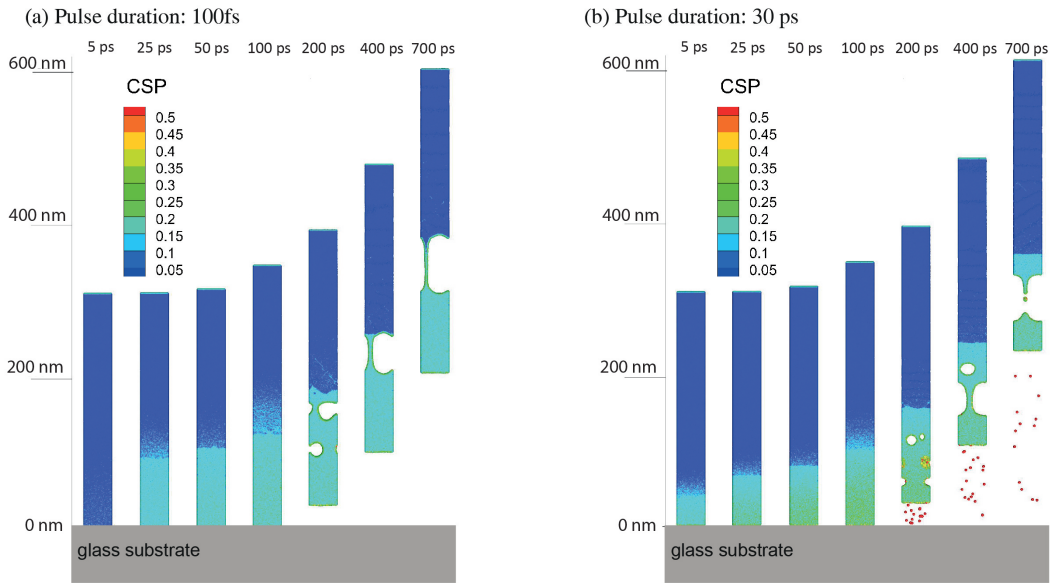

Figure S5: Molecular dynamics simulations of femtosecond and picosecond laser spallation of a 300 nm thin nickel layer excited through the dielectric substrate. The atomic configuration dynamics of the film target during the spallation process due to 100 fs (a) and 30 ps (b) are shown for the selected times. Time zero corresponds to the intensity maximum of the (Gaussian) laser pulse. The atoms are colored by the Central Symmetry Parameter (CSP) for identification of the local crystal structure as follow: solid 0...0.1, liquid 0.1...0.3, vapor >0.50.

perature Model (TTM).[3] The combined MD-TTM model provides a detailed atomic-level description of the kinetics of fast non-equilibrium laser-induced processes including spallation phenomena. At the same time it ensures an accurate description of laser light absorption by the conduction band electrons, fast electron heat conduction and energy transfer to the lattice due to the electron-phonon coupling. The essential concepts of the combined MD-TTM model and its extension for modeling the experimental results are given elsewhere.[4,5]

The computational cell setup in present calculations is similar to the one used for the investigation of melting process in mono- and polycrystalline gold targets.[6] The silica substrate, transparent for the laser pulse, is modelled via an imaginary plane, which weakly interacts with the Ni film and absorbs 30% of the laser-induced pressure waves energy. The simulation of the interaction of a Gaussian laser pulse (wavelength 800 nm, the incident fluence 576 mJ/cm^2=1.2 F_{spall}) with 300 nm Ni target (40x40x300 nm^3), consisting of 30,000,000 atoms, was run across 384 processor cores for the experimental time of 800 ps. The results of the interactions of 100 fs and 30 ps laser pulses with 300 nm Ni film are summarized in Figs. S5(a) and S5(b), where the atomic configuration snapshots of the developing spallation process are shown. The characteristic electron-phonon relaxation time for Ni (for fluences near the melting threshold) is of the order of 10 ps.[7] Since the acoustic relaxation of thermal stress is modified by the presence of the glass substrate, the target is heated under the regime of the internal stress confinement[8] in both cases. However, due to the pulse duration of 100 fs, the strong heating rate results in higher peak pressure values of 30 GPa, developed in the vicinity of the substrate approximately 17 ps after the laser excitation and followed by the subsequent relaxation in a form of compressional longitudinal pressure waves. In the case of a 30 ps laser pulse the highest values of the internal stresses of 18 GPa are developed by the time of 25 ps (after the peak of the laser pulse). The evolution of these giant laser-induced pressure waves and their reflection from the nickel-air interface generate significant tensile stresses of -10 and -5 GPa for the short and long laser pulses, respectively. After reflection these tensile stress pulses propagate back and generate extensive negative unload

upon crossing over inside the molten part of the film at approximately 100 ps after the laser pulse. The relaxation of such tensile stresses in liquid nickel occurs through nucleation of the internal voids inside the melt preceding the spallation onset,[9] see Fig. S5 for 200 and 400 ps time delays. Although the spallation process (i.e. separation of two macroscopic layers of material at a 700 ps time delay) takes place in both cases, the shorter pulse generates stronger temperature gradient that later provides a stronger cooling for the molten part of the film and the nucleation of voids therefore eventually takes place closer to the solid-liquid interface. As a result, one can expect a cleaner laser-treated surface for the shorter pulse without a significant amount of the splashed molten materials. The subsequent material removal is governed by the motion of the nickel-air interface at velocities of about 400 m/s. Depending on the irradiation conditions and the sample's adhesion with the substrate, the spalled layer of liquid nickel detaches from the surface (the situation in Fig. S5) or remains on the surface (as observed in the experiments).

To summarize, the molecular dynamics simulations suggest that fs-laser-spallation occurs at the solid-liquid interface. Ps-laser-spallation should occur somewhere inside the layer of liquid nickel. Nevertheless, given qualitatively the same spallation behaviour, we predict that single picosecond laser pulses can be equally well-suited for the nondestructive pulsed-laser lithography of magnetic materials.

The role of laser focusing and polarization

Being dominated by processes with sharp fluence thresholds, the present nanofabrication technology is not limited by diffraction. For example, the minimum size of spallation cavities (cross-section 3 in Fig. 4), as determined by the SEM, was around 1 μm, i.e. well below the optical resolution limit λ/NA=2.85 μm of a microscope objective used to project the slit on the sample. Nevertheless, producing smaller structures would require a precise control of laser fluence and shot-to-shot pulse energy fluctuations. For this reason, working with

tightly focused optical beams would be advantageous. The latter can be achieved by using high numerical aperture (NA) imaging optics (including immersion objectives with NA>1) and shorter wavelength pump pulses. We envision sub-micrometer lateral dimensions of spallation cavities and periodicities. The latter requires also a strong control of the mechanical vibrations of the moving sample stage. As an alternative route, one could work with mask projection techniques to produce an entire gratings with a sub-micrometer periodicity in a single laser shot.[10] In the case of magnetic materials, variation of light polarization and/or magnetic state of material can be used for fine adjustment of the absorbed laser fluence. The phenomenon of magneto-circular dichroism results in a slightly different absorption of right and left circularly polarized light impinging on a perpendicularly magnetized material. In spite of the small magnitude of this effect (typically 1%), it has been shown to play a dominant role in ultrafast laser-induced magnetization switching of magnetic materials.[11] In the experiments presented in this paper, linearly polarized laser pulses were used, and the mentioned effect didn't play any role.

References

(1) Evico Magnetics GmbH. `http:/evico-magnetics.de`.

(2) Nikulina, E.; Idigoras, O.; Vavassori, P.; Chuvilin, A.; Berger, A. Magneto-optical magnetometry of individual 30 nm cobalt nanowires grown by electron beam induced deposition. *Applied Physics Letters* **2012**, *100*, 142401.

(3) Anisimov, S. I.; Kapeliovich, B. L.; Perel'man, T. L. Electron Emission from Metal Surfaces Exposed to Ultrashort Laser Pulses. *Zh. Eksp. Teor. Fiz.* **1974**, *66*, 776.

(4) Ivanov, D. S.; Zhigilei, L. V. Combined atomistic-continuum modeling of short-pulse laser melting and disintegration of metal films. *Physical Review B* **2003**, *68*, 64114.

(5) Ivanov, D. S.; Kuznetsov, A. I.; Lipp, V. P.; Rethfeld, B.; Chichkov, B. N.; Gar-

cia, M. E.; Schulz, W. Short Laser Pulse Surface Nanostructuring on Thin Metal Films: Direct Comparison of Molecular Dynamics Modeling and Experiment. *Appl. Phys. A* **2013**, *111*, 675.

(6) Ivanov, D. S.; Lipp, V. P.; Rethfeld, B.; Garcia, M. E. Molecular-dynamics study of the mechanism of short-pulse laser ablation of single-crystal and polycrystalline metallic targets. *Journal of Optical Technology* **2014**, *81*, 250–253.

(7) Hohlfeld, J.; Wellershoff, S. S.; Güdde, J.; Conrad, U.; Jähnke, V.; Matthias, Electron and lattice dynamics following optical excitation of metals. *Chem. Phys.* **2000**, *251*, 237.

(8) Ivanov, D. S.; Rethfeld, B. C. The Effect of Pulse Duration on the Character of Laser Heating: Photo-Mechanical vs. Photo-Thermal Damage of Metal Targets. *Appl. Surf. Sci* **2009**, *255*, 9724.

(9) Leveugle, E.; Ivanov, D. S.; Zhigiley, L. V. Photochemical Spallation of Molecular and Metal Targets: Molecular Dynamic Study. *Appl. Phys. A* **2004**, *79*, 1663–1655.

(10) Karstens, R.; Gödecke, A.; Prießner, A.; Ihlemann, J. Fabrication of 250-nm-hole arrays in glass and fused silica by UV laser ablation. *Optics & Laser Technology* **2016**, *83*, 16–20.

(11) Kirilyuk, A.; Kimel, A. V.; Rasing, T. Ultrafast optical manipulation of magnetic order. *Reviews of Modern Physics* **2010**, *82*, 2731–2784.